Chapter 4

Investigation of the role of Sr and Development of Superior Sr doped Hexagonal $BaCoO_{3-\delta}$ Perovskite Bifunctional OER/ORR Catalyst in Alkaline Media

4.1 Introduction:

Without coupling a reliable energy storage system with renewable energy solutions such as solar, wind, and tidal energy, the global energy demand cannot be fulfilled. Oxygen reduction and evolution reactions (ORR and OER) are cornerstones for renewable energy generation devices, high-temperature fuel cells, low-temperature metal−air batteries, and water splitting systems to produce Hydrogen.[1-11] Well-known noble metal oxide-based ORR/OER catalysts such as IrO_2 and RuO_2 are costly, and continuous performance decay restricts their large-scale application on a commercial grade.[12] Recently, low-cost, earth-abundant transition metal oxides gained greater interest to be examined as oxygen electrocatalysts for energy conversion and storage devices.[13-22] Perovskites are of great importance because they exhibit greater cation ordering and order channels of oxygen vacancies resulting in the fast mobility of oxygen ions that improve ORR and OER rates. ABO_3 perovskite is important to structure for the study of the OER/ORR catalysis because of superior electrical and electronic properties that can be tuned systematically by cation substitutions on both the A and B sites with different valance states and ionic sizes [23-32]. The electronic structure of transition metal cations governs the catalytic activity of many important reactions such as oxygen electrocatalysis for energy storage applications.[13-25]However the superior transition metal (3d) and oxygen (2p) orbital overlap at the active sites, and the separation of the surface oxygen's, and the pH dependence for the catalytic OER/ORR activity of the perovskites have been explored a little.[23-25]

The formation of oxygen vacancy is always accompanied by the change of the charge/ionic state and the electronic structure of transition metal ions in the perovskite materials.[23-32] The covalency between the transition metal 3d-band and the oxygen 2p-band depends on the amount of oxygen vacancy and M-O-M bond angle. Higher

oxygen vacancy concentration results in a higher degree of transition metal−oxygen (M-O) covalency that enhances the electrocatalytic activity .[32] Sabatier's principle explains that superior catalytic activity can be achieved when adsorbed species lightly bind to the surface neither so strongly nor too weakly. But the binding strength of oxygen molecules and reaction intermediates is hard to obtain experimentally. Instead, experimental studies have suggested its relation with the intrinsic OER activities of transition metal oxides[23-25] that can be estimated and measured experimentally in the form of the e_g orbital filling of transition metal ions.[32] The e_g orbital filling was established as an OER activity determining parameter with optimal e_g orbital occupancy close to 1 and the $Ba_{0.5}Sr_{0.5}Co_{0.8}Fe_{0.2}O_{3-\delta}$ with nearly e_g^1 configuration was shown as a superior OER catalyst. However, the catalyst suffers severe structural stability issues and readily converts into amorphous structure generating CoO_x motifs under OER conditions.[33-35]

Thus a detailed understanding of electronic structure and materials stability is important to establish a model OER/ORR catalysts. Here, we investigated the role of Sr in Sr-substituted 2H-type $Ba_{1-x}Sr_xCoO_{3-\delta}$ solid solution in the range of composition ($0 \leq x \leq 0.5$) as a model host structure to develop the bifunctional OER/ORR catalyst by altering the cations through A-site substitution. This iso-electronic substitution alters the separation between the B-octahedra blocks and, also the O-Co-O super-exchange bond angle and has a significant effect on the properties that control the oxidation state of cobalt by altering the concentration of oxygen vacancies and the oxygen vacancy migration that make 2H-type $Ba_{1-x}Sr_xCoO_{3-\delta}$ an appealing bifunctional OER/ORR catalyst. Here in this manuscript, we present systematic studies on the substitution of Sr on Ba site in $BaCO_{3-\delta}$ that results in alteration in the crustal structure (M-O-M bond angle and size of the lattice) and electronic structure (electrical conductivity, covalency, and overlap between M(3d) and O(2p) orbitals) of the material resulting in higher OER/ORR activities.

4.2 Materials Synthesis and characterization

The solid-state ceramic synthesis route was used to synthesize the crystalline Sr substituted $BaCoO_3$ solid-state route in general results ma ore thermodynamically stable compound. $BaCO_3$, $SrCO_3$, and $CoCO_3$ were taken as suitable precursors because metathesis (simultaneous decomposition) of carbonates can result in solid

solutions of Ba-Sr. The precursors are taken in stoichiometric ratio and mixed in agate mortar-pestle arrangement for about 40 minutes. The mixture is then fired in a platinum crucible at a temperature of 900 ^{o}C for 15 hours followed by slow cooling. The sample was heated twice with single-phase materials.. The phase formation was studied through Rigaku Miniflex desktop X-ray Diffractometer (XRD) with Cu-Kα radiation (λ = 1.54 Å) in the range 2θ ∼ 20 - 90° with a step size of 0.02°. The structures were refined by the Rietveld refinement method using FULLPROF suite software and hexagonal P63/mmc (space group no. 194) was taken as model structure. The microstructures of the sintered samples were investigated by using a scanning electron microscope (EVO - Scanning Electron Microscope MA15/18). The average grain size was calculated using the linear intercept method. The composition of the compounds was examined by Energy dispersive X-ray (EDX) spectroscopy with a probe attached to the scanning electron microscope. For the single-phase materials, the oxygen deficiency was determined by chemical analysis using redox titration. Aliquots of material were dissolved in hydrochloric acid in the presence of potassium iodide, and the liberated iodine was titrated with sodium thiosulfate using Thyodene as an indicator. Concordant results for y were obtained to within ±0.01. X-ray Photo-electron Spectroscopy (XPS) studies were carried out to investigate the electronic structure of the materials. XPS of the sample was carried out by Thermo Scientific Multilab 2000 instrument using Al Kα radiation operated at 150 W. Binding energies reported here are with reference to C (1s) at 284.5 eV and they are accurate within 0.1 eV.

4.2.1 Electrochemical Studies:

The electrochemical measurements were carried out using nova 2.0 autolab. The catalyst ink was prepared by homogenizing 14 mg of catalyst, 4 mg of carbon material, and 100 μL of Nafion®ionomer solution (0.26 mg mL^{-1}) in 5 mL of water under an ultrasonication bath for 40 min. To investigate the activity of the electrocatalyst, an aliquot of 10 μL of homogenized catalyst ink was deposited by a micropipette onto the surface of glassy carbon (GC) electrode with a geometric area of 7.06 mm^2, and the electrode was polished to a mirror-like appearance and dried under an IR lamp. The catalyst load was typically 396 μg cm^{-2} for the GC.

Linear sweep voltammetry (LSV), cyclic voltammetry (CV), and electrochemical impedance spectroscopy (EIS) in a conventional three-electrode arrangement were used to determine the electrochemical characteristics of the prepared electrocatalysts were measured by Metrohm Autolab (PGSTAT204) equipped with FRA32M module. Electrochemical measurements were analyzed using NOVA software.

Pt was used as a counter-electrode and Ag/AgCl in 3 M KCl was utilized as a reference electrode. All electrode potential values mentioned in this manuscript refer to this Ag/AgCl in the 3 M KCl electrode. Potential conversion for overpotential measurements was done using the following equation-

$$E_{RHE} = E_{Ag/AgCl} + E^{o}_{Ag/AgCl} + 0.059pH \quad (E^{o}_{Ag/AgCl} = 0.210 \text{ for 3 M KCl}) \tag{4.1}$$

$$\text{Overpotential} = E_{RHE} - 1.23 - iR \tag{4.2}$$

R is calculated using EIS measurements. Argon-saturated 1-5 M KOH solution was used as the electrolyte. The electrolyte solutions were freshly prepared before each set of experiments from analytical grade KOH (Lachner, Czech Republic) and deionized water.

4.3 Results and Discussion

4.3.1 Crystallographic characterization

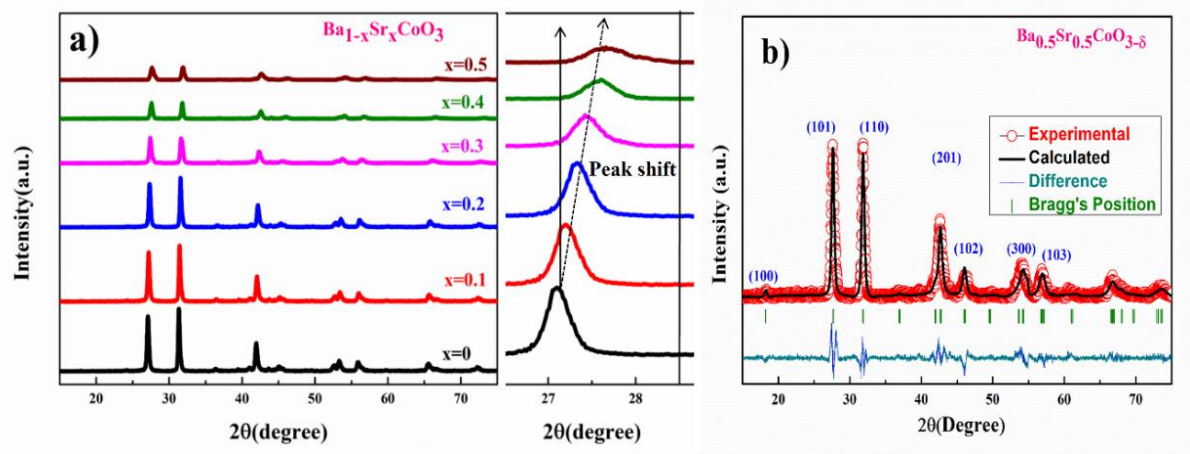

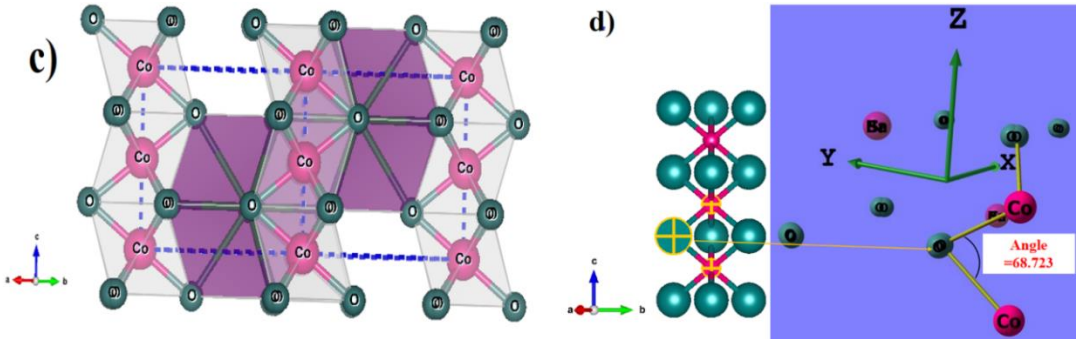

Figure. 4.1. (a) powder XRD pattern of $Ba_{1-x}Sr_xCoO_{3-\delta}$ ($0 \leq x \leq 0.5$) ,(b) Rietveld refinement XRD profile of $Ba_{0.5}Sr_{0.5}CoO_{3-\delta}$ (c) Vesta image of $Ba_{0.5}Sr_{0.5}CoO_{3-\delta}$ and (d) Represent of bond angle of Co-O-Co (between O-2p and Co-3d orbital

Figure .4.1(a) shows the x-ray diffraction plots of $Ba_{1-x}Sr_xCoO_{3-\delta}$ ($0 \leq x \leq 0.5$) solid solutions, showing the synthesis of single-phase Perovskite materials over the whole range of compositions. there is peak broadening with increasing Sr content in $BaCoO_3$ resulting from the residual stress generated in the lattice due to mismatch in the ionic radii of Ba^{2+} and Sr^{2+} **Figure 4.1(b)** shows Rietvel refinement XRD profile of $Ba_{0.5}Sr_{0.5}CoO_{3-\delta}$. Solid solutions were synthesized in single-phase hexagonal perovskite (2H, low-temperature phase, space group P63/mmc) and cell parameters of the respective compositions are presented in Table 1. There is a systematic decrease in the lattice parameter and cell volume of the material with an increase in Sr content in the $BaCoO_{3-\delta}$ lattice. **Figure4.1(c)** presents the **VESTA** image of the unit cell of $Ba_{0.5}Sr_{0.5}CoO_{3-\delta}$. The unit cell is comprised of face-sharing CoO_6 octahedral dimers and CoO_6 octahedral tetramers along the c axis. **Figure4.1 (d)** shows the bond angle between Co-O-Co and it was found that with increasing Sr concentration in $Ba_{1-x}Sr_xCoO_{3-\delta}$ ($0 \leq x \leq 0.5$), Co-O-Co bond angles decrease (Table 4.1).

Table 4.1: Lattice parameter of $Ba_{1-x}Sr_xCoO_{3-\delta}$ ($0 \leq x \leq 0.5$

Sample	a=b (A^0)	c(A^0)	α=β,γ (^{0})	Chi^2	R_{bragg}	R_f	R_{wp}	Co–O–Co angle (deg)
$BaCoO_3$	5.7105(2)	4.4267(6)	90,120	2.81	8.152	7.323	30.6	73.743
$Ba_{0.9}Sr_{0.1}CoO_3$	5.7021(3)	4.4148(5)	90,120	2.87	9.194	8.279	30.9	72.036
$Ba_{0.8}Sr_{0.2}CoO_3$	5.6865(4)	4.3917(4)	90,120	2.76	10.22	7.152	33.6	71.171
$Ba_{0.7}Sr_{0.3}CoO_3$	5.6571(3)	4.3643(2)	90,120	2.606	8.7	5.359	29.6	70.833
$Ba_{0.6}Sr_{0.4}CoO_3$	5.6336(5)	4.3255(4)	90,120	1.97	9.932	7.229	34.4	70.202
$Ba_{0.5}Sr_{0.5}CoO_3$	5.6232(3)	4.3113(5)	90,120	2.19	11.09	7.041	36.7	68.723

4.3.2 Brunauer-Emmett-Teller (BET) analysis

Figure 4.2 represents the BET surface area measurement (N_2 adsorption/desorption isotherms) for $BaCoO_{3-\delta}$ and $Ba_{0.5}Sr_{0.5}CoO_{3-\delta}$. The nitrogen adsorption and desorption isotherm depict the characteristics that correspond to the micro-porous structure. The average pore diameter and calculated BET-specific surface area for $Ba_{0.5}Sr_{0.5}CoO_{3-\delta}$ was found to be 4.12nm and 7.2 m^2/g respectively and for $BaCoO_{3-\delta}$ average pore diameter and specific surface area were found to be 6.09 m^2/g and 3.72 nm respectively

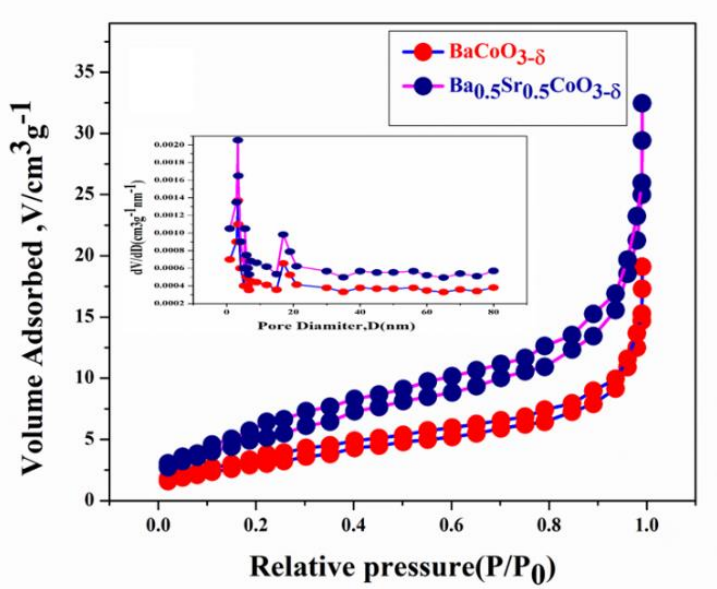

Figure.4. 2 N_2 adsorption/desorption isotherms of $BaCoO_{3-\delta}$ and $Ba_{0.5}Sr_{0.5}CoO_{3-\delta}$

4.3.3 Scanning Electron Microscopy (SEM) with Energy Dispersive X-Ray Analysis (EDX) analysis

. **Figure 4.3 (a)** shows the SEM image that depicts particle size distribution and morphology of the $Ba_{0.5}Sr_{0.5}CoO_{3-\delta}$ sample. As analyzed by **ImageJ** software, dense particles in the range of 150-500 nano-meter sizes with an average particle size approaching 279 nm were visible in the SEM image. **Figure 4.3 (b)** shows the EDX (Energy Dispersive X-ray Analysis) image and the analysis confirms the nominal composition of $Ba_{0.5}Sr_{0.5}CoO_{3-\delta}$.

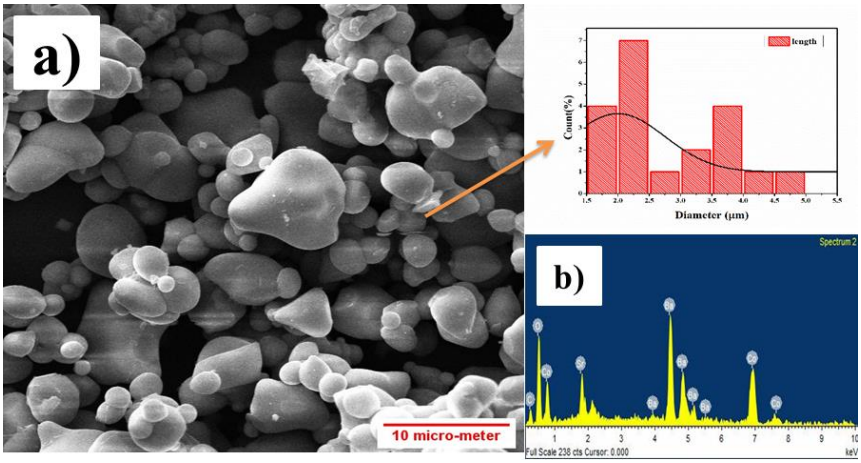

Figure 4.3 (a) SEM image showing the morphology of the $Ba_{0.5}Sr_{0.5}CoO_{3-\delta}$ sample with particle distribution (b) EDX elemental analysis

4.3.4 Transmission electron microscopy (TEM) analysis

TEM images are shown in **Figure 4.4** representing lattice arrangements at localized regions of the powder sample. The inset images represent FFT (Fast Furrier Transformation) and inverse FFT of the sample. The calculated d spacing value was found 0.383nm matches very well with the (101) plane for 2H-perovskite $Ba_{0.5}Sr_{0.5}CoO_{3-\delta}$ phase.

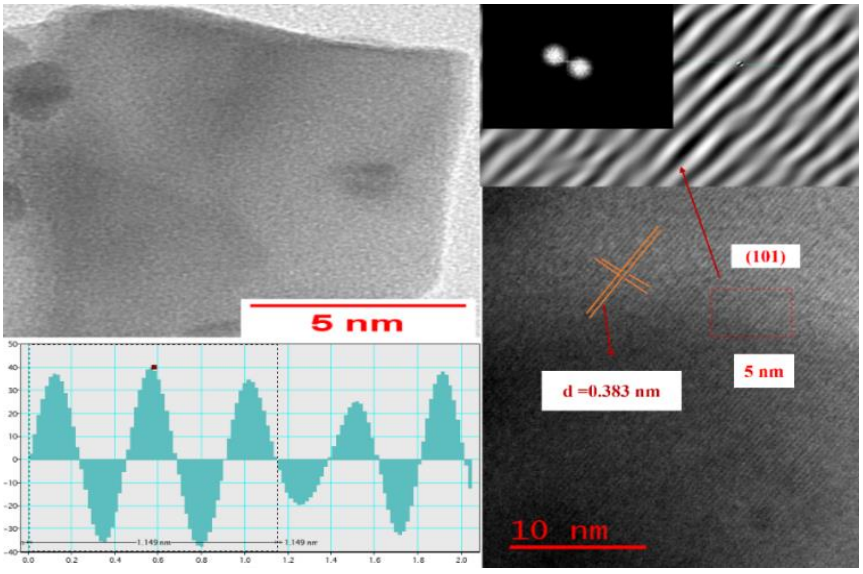

Figure 4.4 TEM image along with HRTEM showing lattice fringes and high-resolution FFT, inverse FFT with d spacing

4.3.5 X-ray photoelectron spectroscopy (XPS) analysis

Figure 4.5(a) shows the survey spectra of the XPS study of the hexagonal $Ba_{0.5}Sr_{0.5}CoO_{3-\delta}$ perovskite sample. The deconvoluted Co(2p) and Ba(3d) spectrums are shown in **Figure 4.5. (b).** The $2p_{3/2}$ and $2p_{1/2}$ peaks marked at 779.65 eV and 794.19 eV respectively belongs to Co^{3+} ions and $2p_{3/2}$ and $2p_{1/2}$ peaks marked at 780.92 eV 796.14 eV belongs to Co^{4+} ions. $2p_{3/2}$ and $2p_{1/2}$ peaks at 779.97 eV and 795.38 eV respectively were assigned for Ba^{2+} ions.

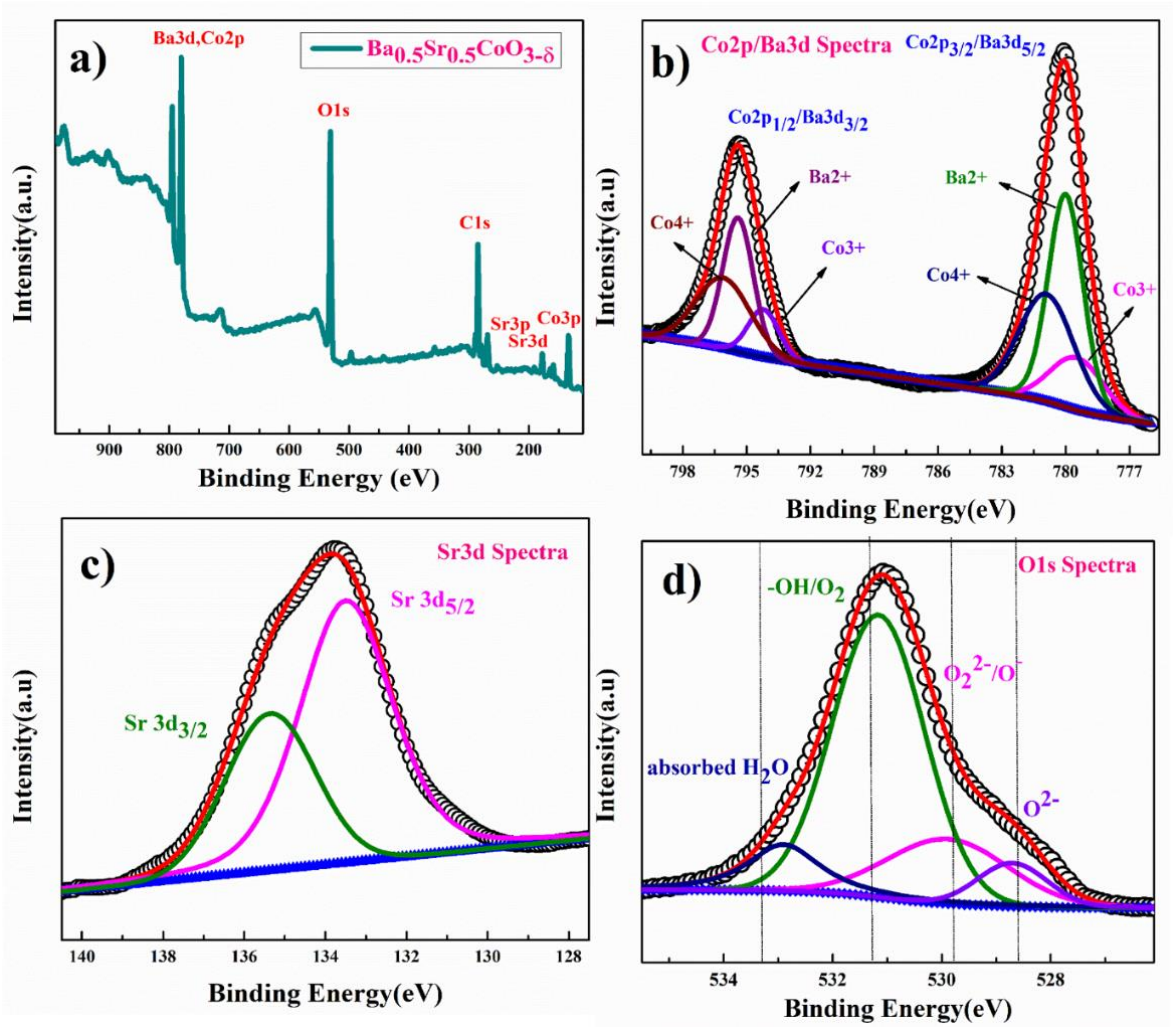

Figure. 4.5 (a) full survey spectra of $Ba_{0.5}Sr_{0.5}CoO_{3-\delta}$ (b) core level of Ba(3d) and Co(2p) spectrum (c) core level of Sr(3d) spectrum (d) core level of O(1s) spectrum.

Figure 4.5(c) shows the Sr3d core level with $3d_{5/2}$ and $3d_{3/2}$ peaks obtained at 133.44eV and 135.36eV respectively. **Figure 4.5(d)** shows the O(1s) core level spectra. The O(1s) spectra are deconvoluted into four characteristic peaks; (1) lattice

oxygen species peak at ≈528.6 eV for O^{2-}, highly oxidative oxygen species peak at ≈529.96 eV for O_2^{2-}/O^-, hydroxyl groups or the surface adsorbed oxygen species peak at ≈531.19 eV for −OH or O_2), and adsorbed molecular water species peak at ≈532.7 eV for H_2O.[47] Previous studies confirms that the oxidative oxygen species ($O_2^{2-}/O-$) formed on the surface of the catalysts are results of the surface oxygen vacancies and lattice oxygen vacancies that play a key role in catalyzing the $O_2^{2-}/O-$ species responsible for superior OER activity of the catalyst.[48-49]

4.3.6 Temperature-dependent resistivity study

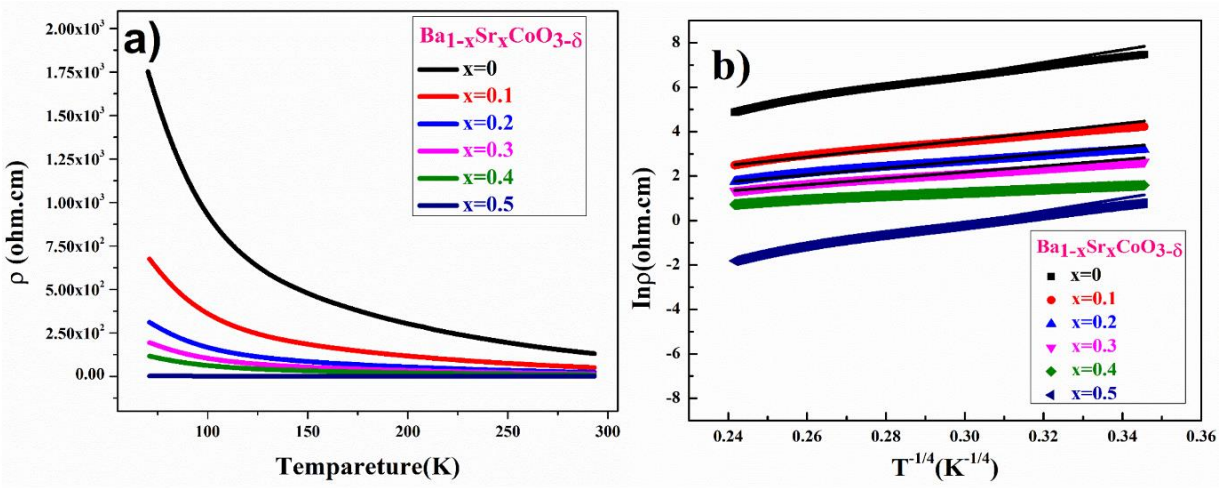

Figure. 4 6 (a) The temperature dependence of electrical resistivity of the 2H-type solid solution $Ba_{1-x}Sr_xCoO_{3-\delta}$ ($0 \leq x \leq 0.5$) as a function of Sr content (b) plot of ln(R) against T-1/4 of the resistivity data

Fig. 4.6 (a) shows the temperature-dependent resistivity (R vs T) plot of 2H-type $Ba_{1-x}Sr_xCoO_{3-\delta}$ ($0 \leq x \leq 0.5$) and at room temperature, the resistivity was found around one order of magnitude lower for $Ba_{0.5}Sr_{0.5}CoO_{3-\delta}$ compared to $BaCoO_{3-\delta}$. The resistivity at 300 K for the $Ba_{0.5}Sr_{0.5}CoO_{3-\delta}$ is approximately 0.163 Ω-cm. The ln(R) vs $T^{-1/4}$ curves shown in **Fig. 4.6 (b)** fit well using equation 3.[37]

$$\sigma (T) = \sigma_0 \exp (T_0 /T)^{1/4} \qquad (4.3)$$

The electrical resistance of the material in the semiconductor region was fitted using Mott's VRH model. Mott VRH conduction is correlated with a high degree of intrinsic lattice disorder and the electrical transport mechanism of the $Ba_{1-x}Sr_xCoO_{3-\delta}$ ($0 \leq x \leq$

0.5) is in a three-dimensional variable range. With increasing Sr content (x), the resistivity of the bulk malarial rapidly decreases.

4.3.7 UV visible spectroscopy analysis

Figure. 4.7 shows the UV-vis absorption spectrum of $Ba_{1-x}Sr_xCoO_{3-\delta}$ ($0 \leq x \leq 0.5$) powder sample. Bandgap decreases with increasing Sr concentration, the highest bandgap 2.62eV was found for $BaCoO_{3-\delta}$, and the lowest bandgap 2.16 eV was obtained for $Ba_{0.5}Sr_{0.5}CoO_{3-\delta}$.

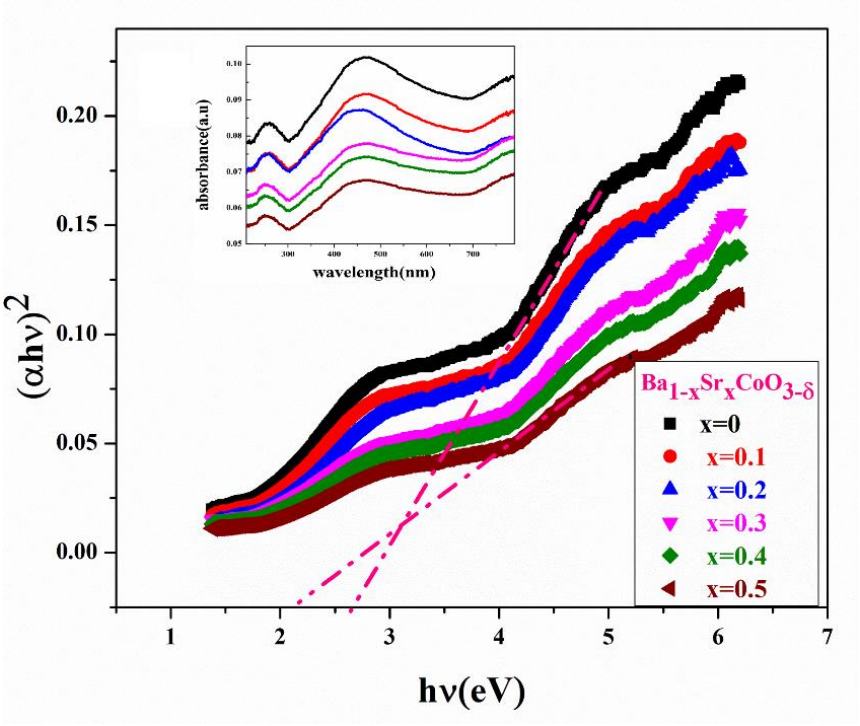

Figure. 4.7 UV-vis absorption spectrum of $Ba_{1-x}Sr_xCoO_{3-\delta}$ ($0 \leq x \leq 0.5$) powder sample

4.3.8 Electronic structure

Figure.4.8 represent the adjustment of the electronic structure and crystal structure of perovskite oxides, thereby making themselves suitable for the superior electrocatalytic activity toward OER and ORR.[38] A-site is generally considered as the inactive site in the ABO_3 type perovskite but it influences the OER/ORR activity of the catalyst indirectly.[39] Here we showed that the introduction of Sr into $BaCoO_3$ stabilizes the crystal structure of the perovskite lattice in such as way that with the decreasing lattice volume, the atoms tend to align in such a way that results in a decrease in Co–

O–Co bond-angle and an increase in Co(3d)-O(2p) hybridization or orbital overlap. Co-O-Co bond angle reaches 68.723° for $Ba_{0.5}Sr_{0.5}CoO_{3-\delta}$ from 73.743° of $BaCoO_{3-\delta}$ (T**able 4.1**). The higher overlap between the occupied O(2p) valence band and the unoccupied Co(3d) band increases the intrinsic catalytic activity of the material.[40]

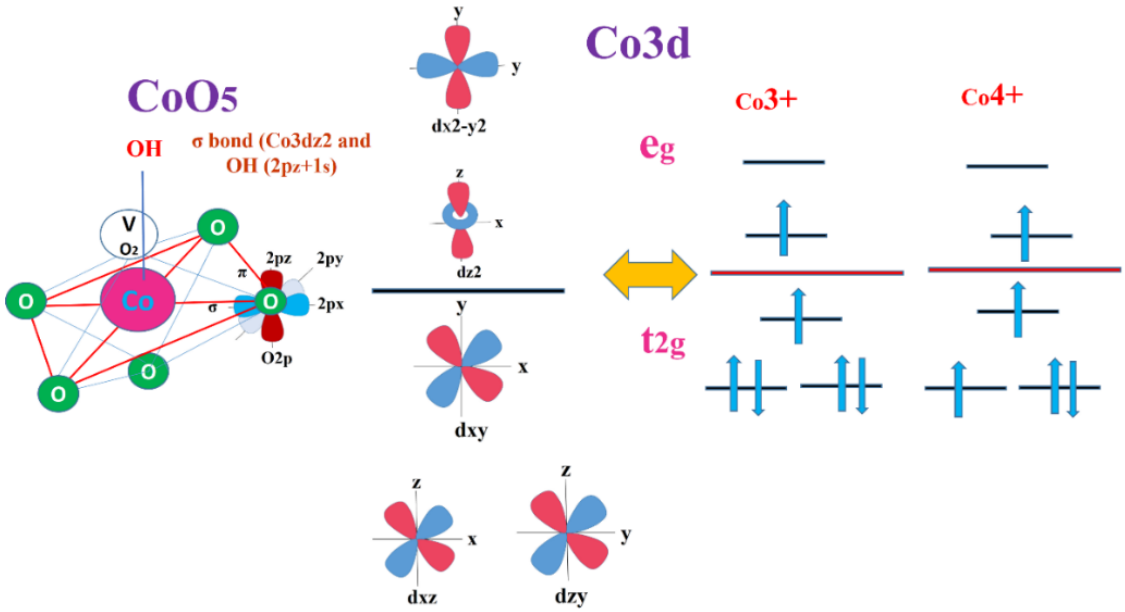

Figure. 4.8 Scheme showing the presence of oxygen vacancies BO_5 octahedral with high overlapping between O(2p) and Co(3d) band.

As shown by XPS studies earlier, due to the presence of Co^{3+} and Co^{4+} in the $Ba_{1-x}Sr_xCoO_{3-\delta}$ sample, the catalytic activity due to the participation of active metal redox ($Co^{3+/4+}$), as well as electronic and ionic properties of the material, are feasibly enhanced. Sr is known to stabilize the high spin $Co^{3+/4+}$ ions in the perovskite structure. Similarly, the existence of high spin Co^{3+} (t_2g^5 eg^1) and/or Co^{4+}(t_2g^4 eg^1) in the perovskite lattice is known to enhance the electrocatalytic activity for both ORR and OER.[41-42] A model of such an active electrocatalyst oxide surface is established; in the oxygen, vacant BO_5 octahedra containing surface oxygen vacancy, the 3d orbital (e_g and t_{2g}) energy split further due to lower symmetry near the surface resulting in more active sites for reaction along (011) planes of $Ba_{0.5}Sr_{0.5}CoO_{3-\delta}$ type oxygen vacant perovskite. [43]

4.3.9 Role of Sr doped in $BaCoO_3$

Figure.4.9 shows the increase in Co(3d)/O(2p) orbital overlap (covalency increases) due to a decrease in Co-O-Co bond-angle with increasing Sr doping. Higher overlap results in higher covalency in Co-O bond resulting in the formation of ligand hole due to a decrease in Fermi level coupled with Co(3d)/O(2p) π* band.[44] Thus pinning of Fermi level due to oxygen vacancies at the top of the Co(3d)/O(2p) π* band results in higher ligand hole concentration required for superior OER activity

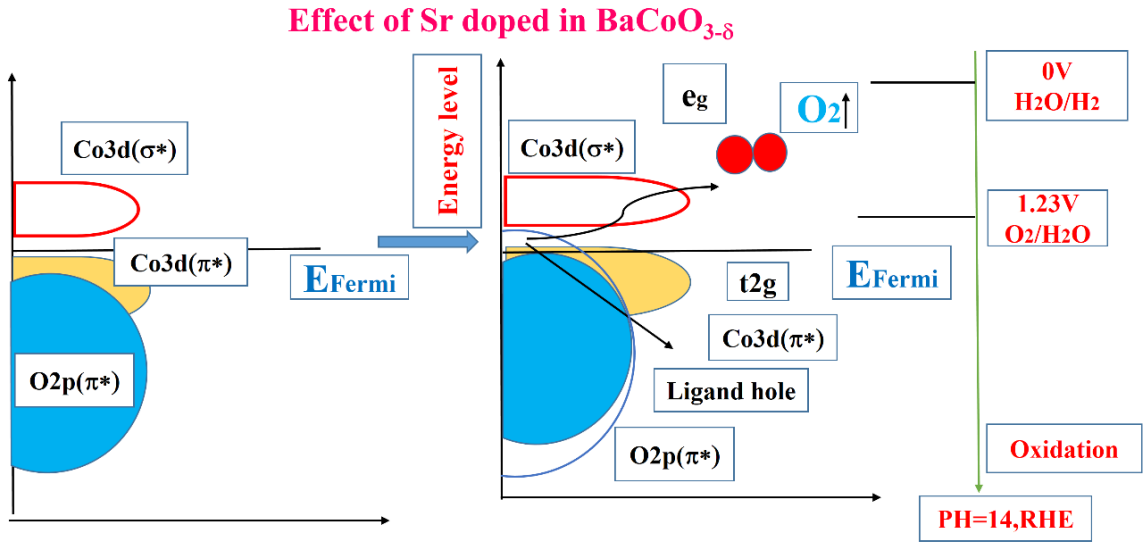

Figure. 4.9 Oxygen vacancies and pinning Fermi level at the top of the Co(3d)/O(2p) π* band

.

4.3.10 Mott–Schottky and flat-band potential

. **Figure 4.10** shows Mott–Schottky plot at 1KHz in between 0 to -1V, the negative slope of the Mott–Schottky plot denotes that $Ba_{1-x}Sr_xCoO_{3-\delta}$ ($0 \leq x \leq 0.5$) materials are p-type (hole) semiconductors. Flat band (E_{fb}) potential is an applied potential at which the Fermi level is pinned at the same energy near the electrolyte redox potential. E_{fb} is an important parameter that provides basic information about the electrochemical interface potential between the electrode and the electrolyte.[43,45] As shown in **Figure 4.10**, the flat band (E_{fb}) potential calculated for $Ba_{0.5}Sr_{0.5}CoO_{3-\delta}$ is found to be 1.557V verse RHE in 0.1M KOH electrolyte

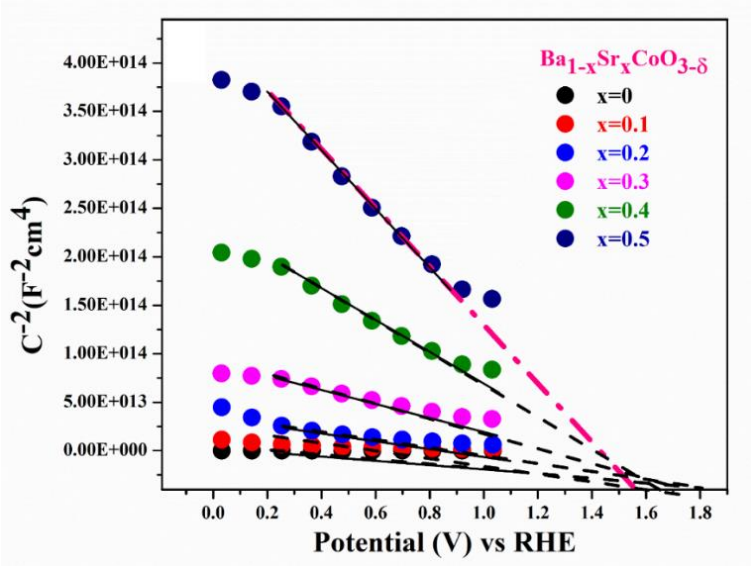

Figure. 4.10 Scheme showing the presence of oxygen vacancies BO_5 octahedral with high overlapping between O(2p) and Co(3d) band. (c) Oxygen vacancies and pinning Fermi level at the top of the Co(3d)/O(2p) π* band

4.3.11 Linear Sweep Voltammetry (LSV) analysis

Figure. 4.11 (a) shows a comparative study of OER and ORR performances of $Ba_{0.5}Sr_{0.5}CoO_{3-\delta}$ and BSCF ($Ba_{0.5}Sr_{0.5}Co_{0.8}Fe_{0.2}O_{3-\delta}$) a well-known model electrocatalyst for OER, the experiments were carried out in oxygen saturated in 0.1M KOH at 3mV/s scan rate, overpotential for BSCF and $Ba_{0.5}Sr_{0.5}CoO_{3-\delta}$ were found to be 370mV and 395mV at 10mA/cm^2 current rate. OER is a charging process, during this process, OH^-/O^{2-} ions are oxidized to O_2 and ORR is discharging process where Oxygen gas is reduced to OH^-/ O^{2-} using an electrocatalyst mounted at the cathode material in the metal-air battery.[22] OER Mechnamism proposed by Bockris on transition metal in perovskite is given below.[43]

$$M^z (Co3d_{z2}) + OH{-}(2p_z{+}1s) \rightarrow M^z{-}OH + e- \quad (4.4)$$

$$M^z{-}OH + OH{-} \rightarrow Mz{-}H_2O_2 + e- \quad (4.5)$$

$$H_2O_2 + OH^- \rightarrow H_2O^- + H_2O \quad (4.6)$$

$$H_2O_2 + H_2O^- \rightarrow H_2O + OH^- + O_2\uparrow \quad (4.7)$$

Figure. 4.11(b) shows Linear sweep voltammogram cycles of $Ba_{1-x}Sr_xCoO_{3-\delta}$ ($0 \le x \le 0.5$) in 0.1M KOH at pH=13 for the OER process. It was observed that incorporation of Sr in $Ba_{1-x}Sr_xCoO_{3-\delta}$ ($0 \le x \le 0.5$) decreases the onset potential to 1.6295V for $Ba_{0.5}Sr_{0.5}CoO_{3-\delta}$ from 1.778V for $BaCoO_{3-\delta}$ versus RHE at 3mA/cm^2

current density. For 50% Sr substitution in $BaCoO_{3-\delta}$, the overpotential reaches 395 mV. **Figure. 4.11 (c)** shows the experiment carried out in oxygen saturated 0.1M KOH electrolyte at 3mV/s scan rate and it was observed that $Ba_{0.5}Sr_{0.5}CoO_{3-\delta}$ electrode showed superior ORR catalyst activity and onset potential was found to be 0.819V vs RHE.

$$ORR = O_2 + 2H_2O + 4e^- \rightarrow 4OH^- \quad (4.8)$$

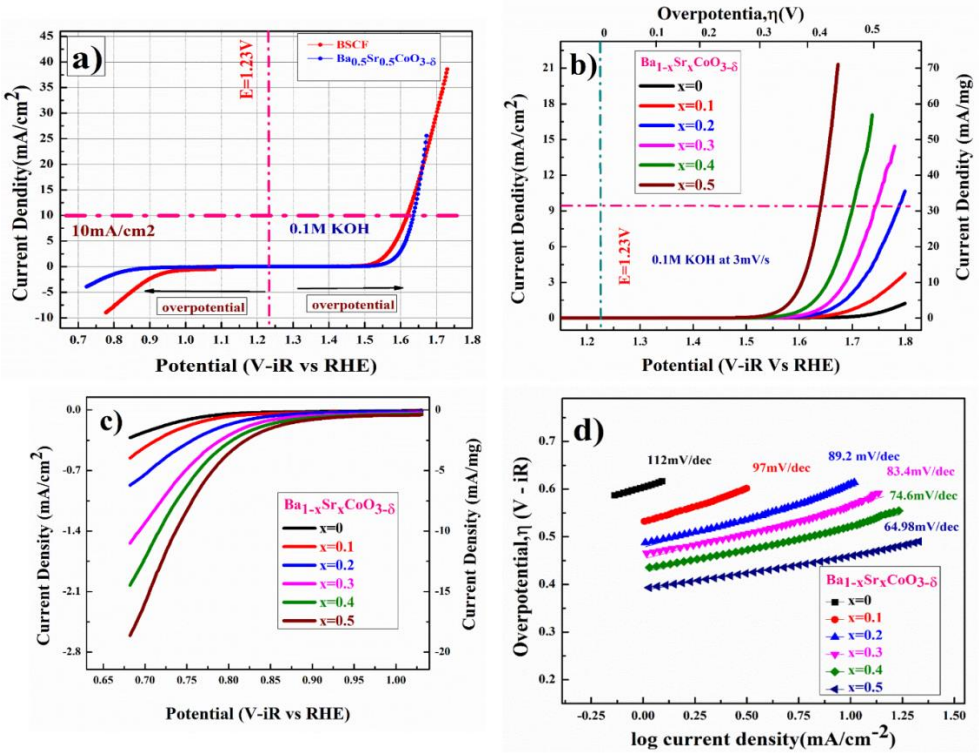

Figure. 4.11 (a) OER and ORR polarization profiles of $Ba_{0.5}Sr_{0.5}CoO_{3-\delta}$, (b) OER polarization profiles for the $Ba_{1-x}Sr_xCoO_{3-\delta}$ ($0 \leq x \leq 0.5$) samples obtained using a 3 mVs^{-1} scan rate, (c) in ORR polarization profiles for the $Ba_{1-x}Sr_xCoO_{3-\delta}$ ($0 \leq x \leq 0.5$) samples obtained using a 3 mVs^{-1} scan rate in O_2 saturated 0.1M KOH solution, (d) respective Tafel plots

Figure. 4.11(d) shows the Tafel plot of $Ba_{1-x}Sr_xCoO_{3-\delta}$ ($0 \leq x \leq 0.5$) catalysts for the OER activities, the polarization curve is plotted between overpotential (η) versus the logarithm of the current density (log i). Tafel plots explain the kinetics of the OER activity. The Tafel slope for $Ba_{1-x}Sr_xCoO_{3-\delta}$ ($0 \leq x \leq 0.5$) are found to be 112, 97, 89.2, 83.4, 74.6 and 64.98 mV dec^{-1} respectively for x = 0, 0.1, 0.2,0.3, 04 and 0.5 samples.

4.3.12 EIS (Electrochemical impedance spectroscopy) analysis

EIS (Electrochemical impedance spectroscopy) measurements were also carried out to evaluate the charge-transfer rate of catalysts. Electrochemical impedance spectra for the $Ba_{1-x}Sr_xCoO_{3-\delta}$ ($0 \leq x \leq 0.5$) at 1.7V vs RHE are shown in **Figure.4.12**. An equivalent circuit fit of EIS data contains a solution resistance (Rs), a charge-transfer resistance (Rct), and a constant-phase element (CPE). A lower Rct value indicates the fastest charge transfer rate and outstanding OER activity. The R_{ct} of $Ba_{0.5}Sr_{0.5}CoO_{3-\delta}$ (21Ω) is much smaller than that of $BaCoO_{3-\delta}$ (69Ω), this demonstrates that with increasing Sr content, the Rct value gradually decreases.

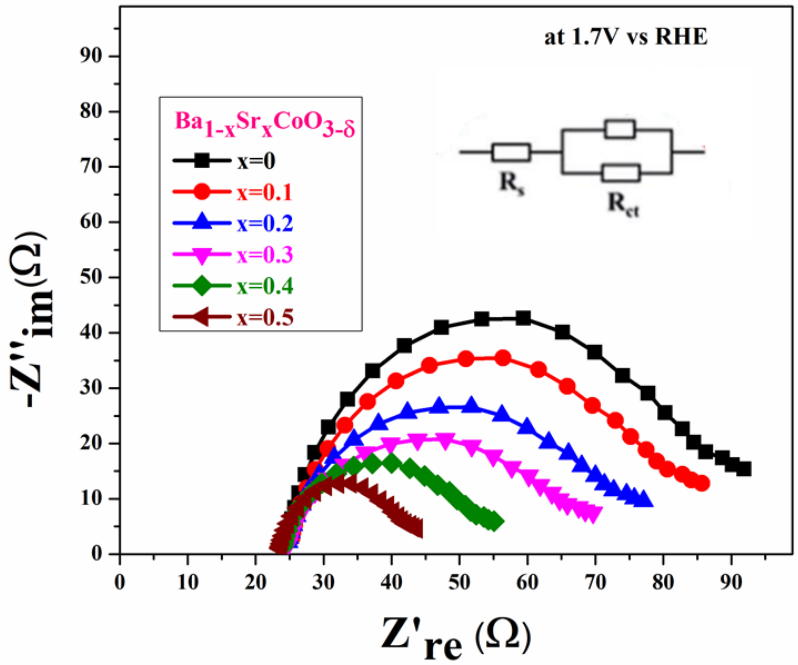

Figure. 4.12 electrochemical impedance spectra for the Ba_{1-x} $Sr_xCoO_{3-\delta}$ ($0 \leq x \leq 0.5$) at 1.7V vs RHE

4.3.13 Cyclic voltammetry perform in different concentration electrolytes

OER performance of the $Ba_{0.5}Sr_{0.5}CoO_{3-\delta}$ at 3 mVs^{-1} scan rate in 0.1, 1, 3, 5, 6M KOH electrolyte is shown in **Figure 4.13** the best performance for $Ba_{0.5}Sr_{0.5}CoO_{3-\delta}$ catalyst was found in 5M KOH electrolyte. In 6M KOH electrolyte, OER performance was decreased, this may be because all adsorption sites will be filled by

OH^- at lower concentration (up to 5M), and the increase in the concentration of the electrolyte further is only contributing to the transformation resistance and have no effect or negative effect on the performance of the catalyst.[18]

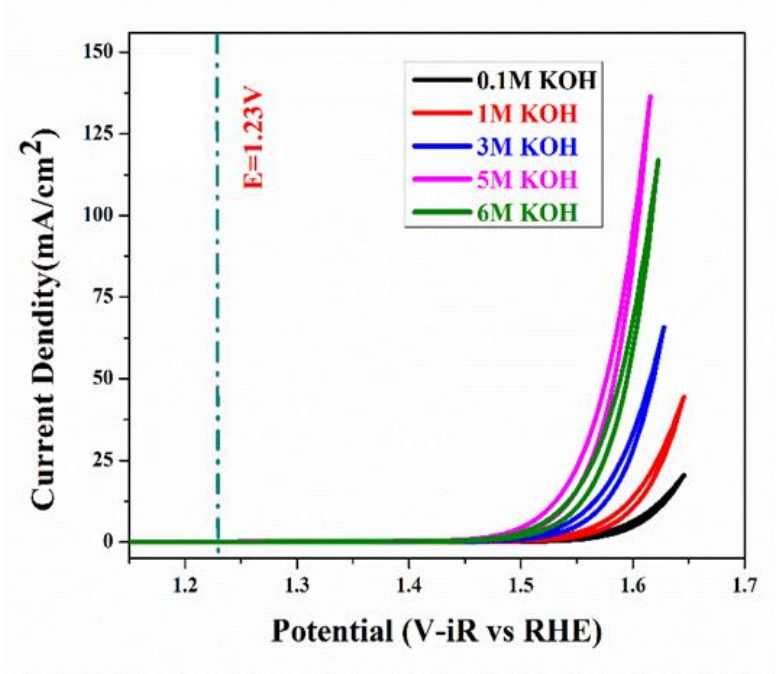

Figure 4.13 OER polarization profiles for the $Ba_{0.5}Sr_{0.5}CoO_{3-\delta}$ at 3 mVs^{-1} scan rate in 0.1, 1, 3, 5, and 6M KOH

4.3.14 Stability performance of cyclic voltammetry analysis

Figure 4.14 shows the stability of $Ba_{0.5}Sr_{0.5}CoO_{3-\delta}$ up to 500 cycles, only about 10% loss in current density is recorded and overpotential shifted to 0.04V higher value after completion of 500 cycles. Durability or long-term stability is also an important criterion to determine the practical applicability of the material. The stability of the $Ba_{0.5}Sr_{0.5}CoO_{3-\delta}$ catalysts was examined by a chronoamperometric experiment.

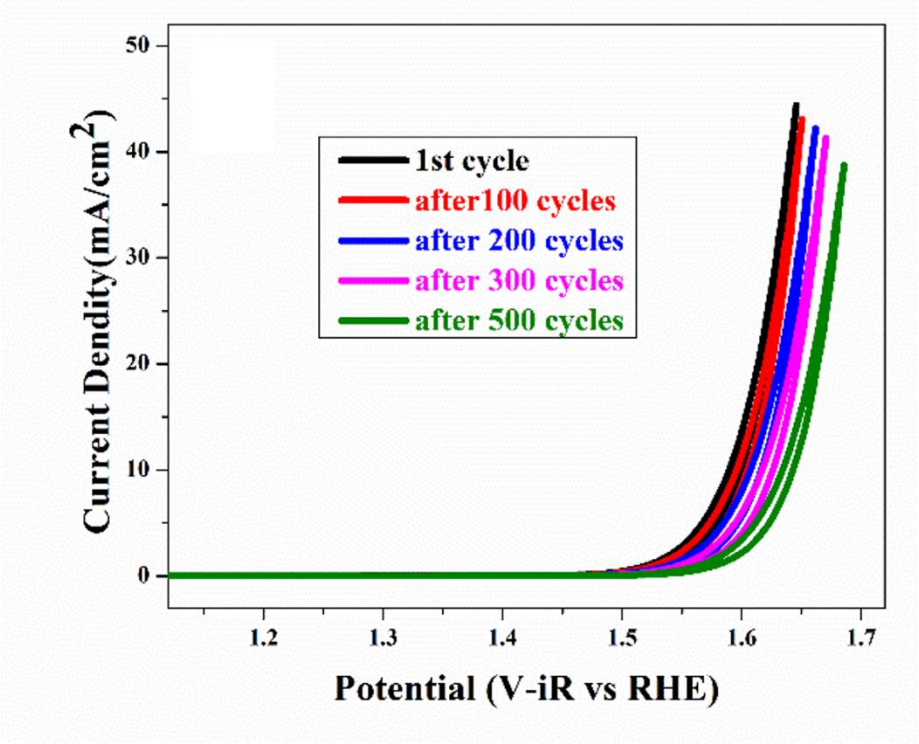

Figure 4.14 Cycles stability up to 500 cycles of $Ba_{0.5}$ $Sr_{0.5}CoO_{3-\delta}$ electrode at 3 mVs^{-1} in 1M KOH

4.3.15 Stability test by chronoamperometric experiment.

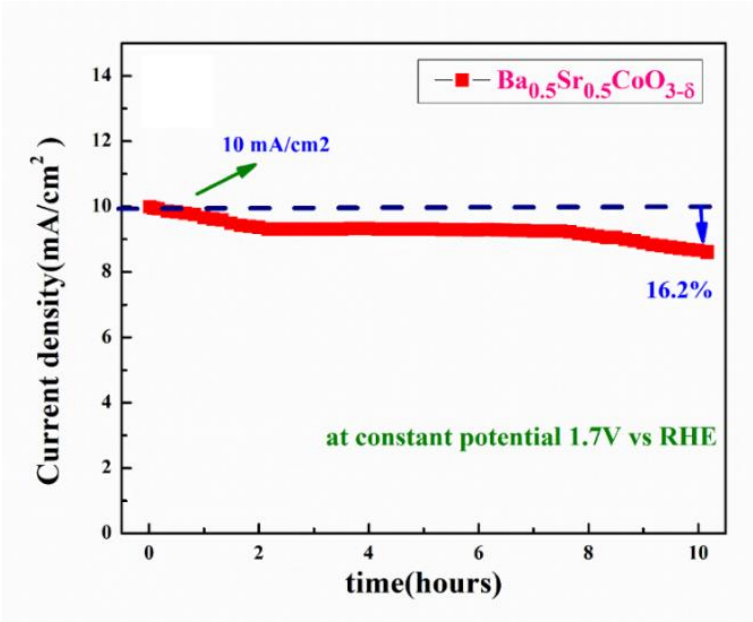

Figure 4.15 Chronoamperometric responses of $Ba_{0.5}Sr_{0.5}CoO_{3-\delta}$ electrode at constant potentials at 1.7 V vs RHE at an initial current density of 10 mA/ cm^2

The stability of the $Ba_{0.5}Sr_{0.5}CoO_{3-\delta}$ catalysts was examined by a chronoamperometric experiment. In **Figure 4.15** $Ba_{0.5}Sr_{0.5}CoO_{3-\delta}$ showed a relatively stable current density at fixed applied potential and a current loss equivalent to ~16% was observed at 1.7V operating voltage vs. RHE in10 hours. These studies demonstrate the superior stability of the 2H-Type perovskite $Ba_{0.5}Sr_{0.5}CoO_{3-\delta}$ catalyst. The well known BSCF showed 94% retention after 1000 cycles.[50] However, the developed hexagonal perovskite ($Ba_{0.5}Sr_{0.5}CoO_{3-\delta}$) catalyst showed 84% retention of the catalytic activity after 10 hour of long cycling The study reveals the direct relation of Physiochemical properties with the inclusion/substitution of Sr in BaCoO3-δ, resulting in superior OER/ORR activity.

4.4 Conclusion

In summary, we synthesized the $Ba_{1-x}Sr_xCoO_{3-\delta}$ ($0 \leq x \leq 0.5$) 2H type low-temperature perovskite phase in P63/mmc space group. Materials phase formation and compositions were confirmed by powder-XRD, TEM, SEM studies, and EDX analysis. The electronic structure of the materials was characterized by XPS, 4-probe conductivity measures, and UV-Visible spectrometer. Incorporation of Sr ion in $Ba_{1-x}Sr_xCoO_{3-\delta}$ ($0 \leq x \leq 0.5$) lattice, facilitates the formation of ligand hole by decreasing the Fermi level position into the Co(3d)/O(2p)π* band. The decrease in the bandgap of the materials and superior electrical conductivity (p-type conduction) suggest a large number of oxygen vacancies or oxygen vacant BO_5 octahedra formation that yields more active sites as this type of oxygen vacancy in perovskite lattice get more reaction surface or active sites because (011) plane contains transition metal (Co) in $Ba_{1-x}Sr_xCoO_{3-\delta}$ perovskite that forms $Co3d_{z2}$ and $OH^{-}(2p_z+1s)$ bond. This accelerates the charge and reactant transportability of the material and oxidative oxygen species O^{2-}/O^{-} on the surface resulting in overall improved bifunctional electrocatalytic oxygen reduction/oxidation activity and long-term stability toward both ORR and OER activity of the material. The onset potential for $Ba_{0.5}Sr_{0.5}CoO_{3-\delta}$ was found to be 1.6295V versus RHE at $10mA/cm^2$ current Density and overpotential reach of 346mV. This onset potential or overpotential matches very well with the calculated flat band (E_{fb}) potential (1.557V) for $Ba_{0.5}Sr_{0.5}CoO_{3-\delta}$ verse RHE in 0.1M KOH electrolyte from Mott–Schottky plot.